**Atmospheric
Chemistry
and Physics
Discussions**

Aerosol mixing-state, hygroscopic growth and cloud activation efficiency during MIRAGE 2006

S. Lance[1,2,3], T. Raatikainen[3], T. Onasch[4], D. R. Worsnop[4], X.-Y. Yu[5],
M. L. Alexander[5], M. R. Stolzenburg[6], P. H. McMurry[6], J. N. Smith[7], and
A. Nenes[3,8]

[1]Chemical Sciences Division, Earth System Research Laboratory, National Oceanic and
Atmospheric Administration, Boulder, CO, USA
[2]Cooperative Institute for Research in Environmental Sciences, University of Colorado,
Boulder, CO, USA
[3]School of Earth and Atmospheric Sciences, Georgia Institute of Technology, Atlanta, GA,
USA
[4]Aerodyne Research Inc., Billerica, MA, USA
[5]Pacific Northwest National Laboratory, Richland, WA, USA
[6]University of Minnesota, Minneapolis, MN, USA
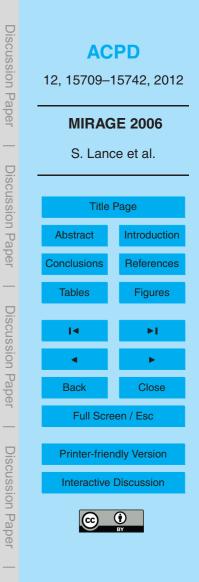[7]National Center for Atmospheric Research, Boulder, CO, USA
[8]School of Chemical and Biomolecular Engineering, Georgia Institute of Technology, Atlanta,
GA, USA

Title Page

Abstract   Introduction

Conclusions   References

Tables   Figures

◄◄   ►►

◄   ►

Back   Close

Full Screen / Esc

Printer-friendly Version

Interactive Discussion

Abstract

Observations of aerosol hygroscopic growth and CCN activation spectra for submicron particles are reported for the T1 ground site outside of Mexico City during the MIRAGE 2006 campaign. κ-Köhler theory is used to evaluate the characteristic water uptake coefficient, κ^*, for the CCN active aerosol population using both size-resolved HTDMA and size-resolved CCNc measurements. Organic mass fractions, f_{org}, are evaluated from size-resolved aerosol mass spectrometer (AMS) measurements, from which κ_{AMS} is inferred and compared against κ^*.

Strong diurnal profiles of aerosol water uptake parameters and aerosol composition are observed. We find that new particle formation (NPF) events are correlated with an increased κ^* and CCN-active fraction during the daytime, with greater impact on smaller particles. During NPF events, the number concentration of 40 nm particles acting as CCN can surpass by more than a factor of two the concentrations of 100 nm particles acting as CCN, at supersaturations of 0.51 %±0.06 %. We also find that at 06:00–08:00 in the morning throughout the campaign, fresh traffic emissions result in substantial changes to the chemical distribution of the aerosol, with on average 65 % externally-mixed fraction for 40 nm particles and 30 % externally-mixed fraction for 100 nm particles, whereas at midday nearly all particles of both sizes can be described as internally-mixed.

Average activation spectra and growth factor distributions are analyzed for different time periods characterizing the daytime (with and without NPF events), the early morning "rush hour", and the entire campaign. We show that κ^* derived from CCNc measurements decreases as a function of size during all time periods, while the CCN-active fraction increases as a function of size. Size-resolved AMS measurements do not predict the observed trend for κ^* versus particle size, which can be attributed to unresolved mixing-state and the presence of refractory material not measured by the AMS. Measured κ^* typically ranges from 0.2 to 0.35, and organics typically make up 60–85 % of the aerosol mass in the size range studied. Despite some disagreement between κ_{AMS}

and κ_{CCNc}, we show that κ_{AMS} is able to describe CCN concentrations reasonably well, especially at the highest CCN concentrations. This is consistent with other CCN studies carried out in urban environments, and is partly due to the fact that the highest CCN concentrations occur during the daytime when the aerosol is internally-mixed and the
5 organic fraction is relatively low. During the early morning rush hour, however, failing to account for the aerosol mixing-state often results in systematic overestimation of CCN concentrations by 50–100 %.
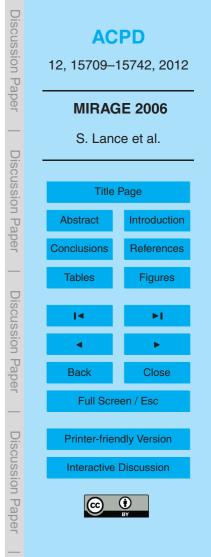
1 Introduction

The greater Mexico City area is home to $\sim$20 million people, making it one of the
10 most populous metropolitan areas in the world. The city is situated on a dry lake bed at an altitude of $\sim$2200 m and is surrounded by mountains, resulting in a unique environment with dense atmospheric pollutants trapped at high-altitude, where rapid photochemical oxidation can take place. Understanding the sources and evolution of particulate matter in Mexico City are two important objectives for the international
15 investigation within and downwind of Mexico City called MILAGRO (Megacity Initiative: Local and Global Research Observations, http://www.ucar.edu/communications/ quarterly/spring06/milagro.jsp). A subset of this study, called MIRAGE (Megacities Impacts on Regional and Global Environments), included measurements at several ground-based sites (Fast et al., 2007; Molina et al., 2010) over the month of March
20 2006.
The impact of aerosols on climate, visibility and human health depends on the degree to which particles swell in humid environments and the efficiency with which particles act as cloud condensation nuclei (CCN). The measurements presented here focus on the water uptake properties of ambient aerosol outside of Mexico City at the Univer-
25 sity of Tecamac (T1) ground site from 16–31 March 2006. Measurements under both subsaturated (relative humidity, RH <100 %) and supersaturated (RH > 100 %) conditions were obtained, from which the evolution of the aerosol mixing-state is analyzed

Full Screen / Esc

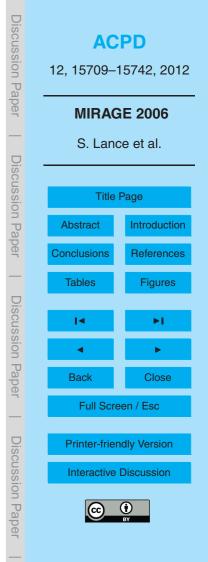Printer-friendly Version

Interactive Discussion

in detail. In the following analysis, we discuss the dominant processes impacting the aerosol water uptake properties (e.g. new particle formation events, primary emissions and aging of the aerosol).

2   Methods

2.1   Measurements and instrumentation

Ambient air was sampled continuously through an inlet above the roof of a portable laboratory operated by the National Center for Atmospheric Research. An inline impactor located inside the laboratory removed particles greater than 1 µm, and was cleaned twice each day due to the heavy dust load. The sample line was split immediately after the impactor between two independent systems to measure size resolved CCN activation spectra (the fraction of particles that form cloud droplets for a given dry particle size and water vapor supersaturation), and aerosol hygroscopicity (the equilibrium uptake of water by particles exposed to a relative humidity (RH) <100 %). Particles with 40–100 nm diameter were targeted because the threshold activation diameter (corresponding to the critical supersaturation where 50 % of CCN-active particles are activated) often falls within this size range for typical cloud supersaturations (Andreae and Rosenfeld, 2008).
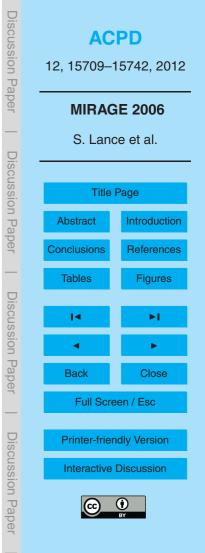
To obtain size-resolved CCN activation spectra, a similar experimental setup to Cerully et al. (2011) was used. The sampled aerosol was electrostatically classified with a differential mobility analyzer (nanoDMA, TSI 3085) (Chen et al., 1998) using a 210-Po neutralizer. Activation spectra were obtained for four classified dry particle sizes (nominally 40, 60, 80 and 100 nm): 41.7±0.48 nm, 62.5±0.69 nm, 83.4±0.91 nm and 104±1.1 nm standard deviation. Downstream of the nanoDMA, the flow was split between a Droplet Measurement Technologies (DMT) cloud condensation nuclei counter (CCNc) (Roberts and Nenes, 2005; Lance et al., 2006; Rose et al., 2008) and a TSI 3760 Condensation Particle Counter (CPC) modified with a critical orifice at the exhaust

line. The nanoDMA was operated with a sheath flow of $6 \, \text{L min}^{-1}$, while the CCNc and CPC were operated with 0.75 and $1.5 \, \text{L min}^{-1}$ flow rates, respectively, resulting in a nanoDMA sheath-to-aerosol flow ratio (SAR) of $\sim$2.7 and a CCNc SAR of 10. The low nanoDMA SAR (comparable to that used by McMurry et al. (2009)) resulted in a trans-fer function that allowed transmission of particles 35.7–48.8 nm at the 40 nm setpoint and 89–124 nm at the 100 nm setpoint (for singly charged particles only). A higher sheath flow rate could not have been used to increase the nanoDMA SAR, because of the voltages required to classify particles of $\sim$100 nm diameter with the nanoDMA. The colder end of the CCN column was maintained at $T_c = 24.0 \pm 1.38\,^{\circ}\text{C}$, while the warmer end was maintained at T_h to obtain ΔT ranging from from $1.87 \pm 0.032\,^{\circ}\text{C}$ to $13.7 \pm 0.038\,^{\circ}\text{C}$, corresponding to a range of supersaturations $\sim$0.07–1.05 %. For refer-ence, ambient cloud supersaturations are generally <1 % (Seinfeld and Pandis, 1998). Every 3 min, the CCNc supersaturation was increased by 0.12 % and the nanoDMA upstream of the CCN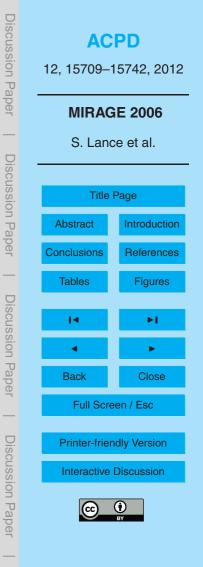c stepped through the same four particle sizes. We exclude the first 56 seconds in every 3 minute period, to allow the instrument supersaturation to reach steady state. Excluding 20 seconds after each change in the particle size set-point leaves 16 seconds of CCN and CN concentration measurements to average for one "activated fraction". The 40 nm and 60 nm data at the lowest supersaturation set-point are also excluded resulting in a total of 4.8 min of measurements excluded from our analysis every time supersaturation was changed from the highest to the lowest setting starting the 30 min cycle over again. This is comparable to the 5 min of mea-surements excluded by Rose et al. (2010), and was deemed sufficient for the higher CCNc flow rate used in our study ($0.75 \, \text{L min}^{-1}$ instead of $0.5 \, \text{L min}^{-1}$). Thus, measure-ments at 8 and 9 supersaturation settings are obtained for 40–60 nm and 80–100 nm particles, respectively. The particle concentration measured for a 100 nm slice of the particle size distribution ranged from 1 to $1000 \, \text{cm}^{-3}$ during the study, indicating that the airmass was often quite polluted. Without size classification, water vapor depletion would have been a significant problem in the CCNc (Lathem and Nenes, 2011).

To measure the aerosol hygroscopicity, a humidified tandem differential mobility analyzer (HTDMA) (Rader and McMurry, 1986) was built and deployed. The HTDMA was maintained at a controlled temperature of 32.9±0.55 °C using a recirculating air bath. The inlet and central humidity were controlled by mixing moist and dry compressed air supplies to the shell of multi-tube Nafion humidifiers. Humidity was monitored at eight locations within the HTDMA (at the inlet and outlet of both the sample and sheath flows in both DMAs) with Vaisala humidity probes (HMM30C), which have a specified accuracy of ±2 % RH at RH <90 %. The measured humidity at the inlet to DMA2 was maintained at 88.2 %±1.2 % RH throughout the study, while the inlet to DMA1 was maintained at <5 % RH. However, calibrations with 20–100 nm NaCl aerosol suggest that the humidity was slightly higher than measured, with an average calibrated RH of 90.8 %±1.11 % based on an expected growth factor of 1.3 for NaCl (Petters and Kreidenweis, 2007). DMA1 classified a different particle size (20, 40, 60, 80 and 100 nm) every 6 min, while DMA2 scanned in 30 10-s steps to obtain the size distribution after humidification, covering the range of growth factors from 0.6 to 2.8. The sheath flows were set to 7 L min^{-1}, resulting in a SAR of 6.5 for both DMAs. Each time the voltage on DMA2 was increased, the first 8 seconds of data were excluded and measurements were made over the remaining 2 s. Each time the voltage on either DMA was returned from the maximum back to the minimum setpoint, an additional 60 seconds of data were excluded.

Ambient size-resolved mass distribution measurements were obtained using a Time-of-Flight Aerosol Mass Spectrometer (TOF-AMS) (Cross et al., 2009). In the Particle Time-of-Flight (PTOF) mode of the AMS, a mechanical chopper modulates the sampled particle beam, and 5 min average mass spectra are obtained as a function of particle vacuum aerodynamic diameter (d_{va}) (Jayne et al., 2000). The non-refractory particulate mass distributions (i.e., organics, sulfates, nitrates, ammonium, and chloride) were binned logarithmically using 32 bins per decade over the d_{va} range 20–2000 nm and normalized to the corresponding mass loadings measured using the Mass Spectrum (MS) mode of the AMS. d_{va} was converted to mobility diameter for

comparison to the water uptake measurements by dividing by an assumed particle density, $\rho_p = 1.45\,\mathrm{g\,m^{-3}}$ (Salcedo et al., 2006) and dynamic shape factor of 1.0 (De-Carlo et al., 2004).

2.2 Analysis method

2.2.1 CCN measurements and derivation of κ_{CCNc}

Every 30 min we obtained activation spectra for four particle sizes, covering a range in supersaturations from 0.07 % to 1.05 %. A single point on an activation spectrum indicates the fraction of particles with a critical supersaturation (s_c) less than or equal to the instrument supersaturation (s), where $s = S - 1$ (usua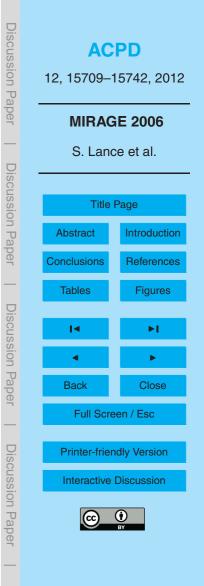lly expressed as a percentage) and S is the saturation ratio. Each point on a single activation spectrum was taken within 3 minutes of the adjacent point. We fit the activation spectra to a sigmoidal function of the following form:

$$R_a(s) = \frac{E}{1 + (s/s^*)^{-C}} \tag{1}$$

where $R_a(s)$ is the fraction of classified particles that activate at critical supersaturations less than or equal to s, E is the upper asymptote of the sigmoid (indicating the fraction of CCN-active particles), s^* is the location of the inflection point (indicating the "characteristic" critical supersaturation of the CCN-active particles) and C is proportional to the slope (indicating the degree of physical and chemical heterogeneity of the CCN-active particles).

The normalized sigmoidal function, $R_a^*(s)$, is a 2 parameter log-logistic function (Ashkar and Mahdi, 2006), and describes the chemical characteristics of the activated particles.

$$R_a^*(s) = \frac{R_a(s)}{E} = \frac{1}{1 + (s/s^*)^{-C}} = \frac{(s/s^*)^C}{(s/s^*)^C + 1} \tag{2}$$

Differentiating $R_a^*(s)$ yields the probability distribution of particles activating at $s = s_c$ (Ashkar and Mahdi, 2006; Lance, 2007):

$$p(s_c) = \frac{d(R_a^*(s_c))}{ds} = \left(\frac{C}{s^*}\right) \frac{(s_c/s^*)^{C-1}}{\left(1 + (s_c/s^*)^C\right)^2} \tag{3}$$

If all particles in the aerosol population have a single critical supersaturation, s^*, $p(s_c)$ would be a delta function and R_a^* would be a step function. Heterogeneity in the chemical composition and particle size both contribute to broadening of $p(s_c)$ and the finite slope parameter, C, of the activation spectrum (Lance, 2007; Cerully et al., 2011).

To unravel these contributions and obtain a measure of the chemical heterogeneity, we express critical supersaturation in terms of hygroscopicity parameter κ as follows. The relationship between κ, d_p and s_c for an individual particle is described by κ-Köhler Theory (Petters and Kreidenweis, 2007):

$$\ln(s_c + 1) = \left(\frac{4A^3}{27\kappa d_p^3}\right)^{1/2} \tag{4}$$
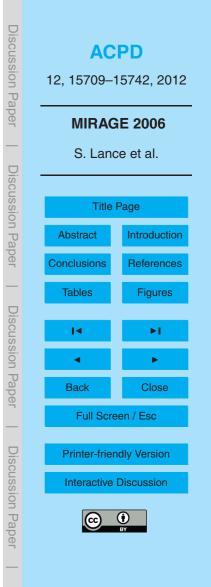
where $A = 4M_w \sigma_w/(RT\rho_w)$, M_w, σ_w and ρ_w are the molecular weight, surface tension and density of pure water, R is the universal gas constant, $T = (T_c + T_h)/2$ is the average temperature within the CCNc column and d_p is the particle dry diameter (assumed to be spherical). s^* can then be expressed, using Eq. (4), in terms of a "characteristic" hygroscopicity, κ^*:

$$\kappa^* = \frac{4A^3}{27 d_p^3 (\ln(s^* + 1))^2} \tag{5}$$

In this study, measured values of κ^* are referred to as κ_{CCNc}. For direct comparison with other CCN activity studies, we assume in the calculation of κ^* that there is no

surface tension depression from surface active compounds, although filter samples from the T1 site during the same time period, extracted to CCN-relevant concentrations, showed surface tension depression of 10–15 % compared to pure water, which can introduce a 30–40 % uncertainty in the value of κ (Padró et al., 2010). Note that there may be significant covariance between κ_{CCNc} and surface tension, such that the effects of aerosol composition and surface tension cannot be distinguished without additional observational constraints.

If the aerosol population is monodisperse, then $p(\kappa)$ has a width directly related to the chemical heterogeneity of the aerosol, and can be described using the sigmoidal fit to the activation curve by directly substituting s_c (in terms of κ, Eq. 4) into Eq. (3). However, we cannot neglect the finite width of the DMA transfer function, and we account for its effect on $p(\kappa)$ through application of the well known error propagation formula:

$$\sigma_{s_c}^2 = \left| \frac{\partial s_c}{\partial d_p} \right|^2 \sigma_{d_p}^2 + \left| \frac{\partial s_c}{\partial \kappa} \right|^2 \sigma_\kappa^2 + 2 \frac{\partial s_c}{\partial d_p} \frac{\partial s_c}{\partial \kappa} \text{cov}_{d_p \kappa} \tag{6}$$

where $\sigma_{s_c}^2$ represents the total variance of $p(s_c)$ about s^*; $\sigma_{d_p}^2$ and σ_κ^2 are the contribution of d_p and κ variances, respectively, to $\sigma_{s_c}^2$. The covariance term, $\text{cov}_{d_p \kappa}$, in Eq. (6) is assumed to be negligible, a valid assumption if d_p and κ are independent over the width of the DMA transfer function. The remaining terms can be derived from Taylor Series expansion of Eq. (4) ($S_c = s_c + 1 = \exp(x) \approx 1 + x$, where $x = \left(\frac{4A^3}{27\kappa d_p^3} \right)^{1/2} \approx s_c$, therefore $\partial s_c / \partial d_p = -(3/2)(s_c / d_p)$ and $\partial s_c / \partial \kappa = -(1/2)(s_c / \kappa)$). Equation (6) then simplifies to:

$$\frac{\sigma_{s_c}}{s_c} = \sqrt{\left(\frac{3}{2} \frac{\sigma_{d_p}}{d_p} \right)^2 + \left(\frac{1}{2} \frac{\sigma_\kappa}{\kappa} \right)^2} \tag{7}$$

σ_{s_c} is determined from the log-logistic sigmoidal fit (Ashkar and Mahdi, 2006) for $C > 2$:

$$\sigma_{s_c} = \left((s^*)^2 \left(\frac{2\pi/C}{\sin(2\pi/C)} - \frac{(\pi/C)^2}{\sin^2(\pi/C)} \right) \right)^{1/2} \tag{8}$$

σ_κ, which is the dispersion in hygroscopicity (and expresses the aerosol chemical heterogeneity), can then be determined from Eq. (7), given estimates for σ_{d_p} (based on the nanoDMA transfer function), σ_{s_c} (from Eq. 8), and κ^* (from Eq. 5).
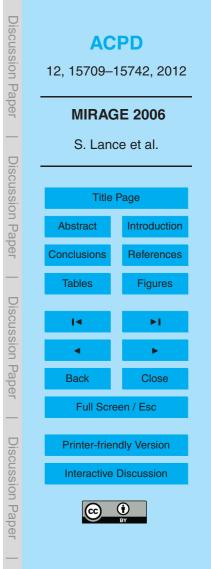
To evaluate the effect of mixing-state on CCN concentrations (Sect. 3.4), we calculate CCN activation spectra as a function of time given different assumptions for E, σ_κ and κ^*. The fraction of particles with $s_c < s$ is calculated for each point in the CCN activation spectra, and subsequently multiplied by E and by the classified particle concentrations. The measured and simulated CCN concentrations are inverted to determine $n_{CCN}(d_p, s) = dN_{CCN}/d\log d_p$ by accounting for charging efficiency, subtracting the maximum expected contribution from doubly and triply charged particles (which ranges from 2.9 % to 16.1 % of measured particles for the 40 and 100 nm setpoints, respectively) and by accounting for the width of the nanoDMA transfer function.

2.2.2 Derivation of κ_{HTDMA}

κ is derived from the HTDMA measurements according to the dependence on growth factor (GF), as given by Petters and Kreidenweis (2007):

$$\kappa(GF, d_p) = \frac{(GF^3 - 1)\exp\left(\frac{A}{d_p GF}\right)}{RH} - GF^3 + 1 \tag{9}$$

where GF is the ratio of particle size selected by DMA2 to particle size selected by DMA1 (corresponding to Z_p and Z_p^*, respectively, as defined by Rader and McMurry (1986)).

Measured GF distributions are corrected for broadening due to the DMA transfer functions using a procedure called TDMAfit (Stolzenburg and McMurry, 1988). The parameters calculated by TDMAfit for a given measured GF distribution are the mean diameter growth factor (G_i), the diameter spread factor (S_i), and the aerosol number concentration (N_i) for each of up to three Gaussian GF modes. Inverted GF distributions, $p(GF)$, are calculated using Eq. (10). Only TDMAfit results for $\chi^2 < 500$ are reported (Rader and McMurry, 1986).

$$p(GF) = \frac{\sum_i^3 \frac{N_i}{\sqrt{2\pi}S_i G_i} \exp\left[-\frac{1}{2}\frac{(GF-G_i)^2}{(S_i G_i)^2}\right]}{\sum_i^3 N_i} \tag{10}$$
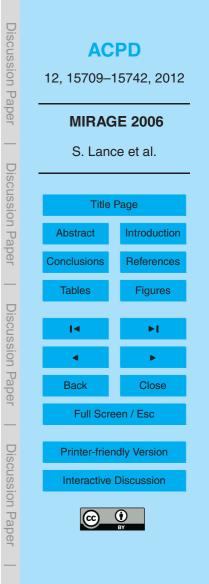
The "characteristic" hygroscopicity, κ_{HTDMA}, is determined by taking a number weighted average of $p(GF)$, starting with the most hygroscopic particles until the fraction of particles measured by the HTDMA included in the average equals the CCN-active fraction (E). This method for calculating the characteristic hygroscopicity parameter, as given by Eq. (11), is different from the methods reported by Su et al. (2010), in that the externally-mixed non-CCN-active particles are not included in the average.

$$\kappa_{HTDMA} = \int_{GF_0}^{GF_{max}} p(GF)\kappa(GF,d_p)d\,GF \tag{11}$$

where GF_0 is the limit of integration required to satisfy the criteria $\int_{GF_{max}}^{GF_0} p(GF)d\,GF = E$. We subsequently compare κ_{HTDMA} and κ_{CCNc} directly, expecting that they represent the same population of particles.

2.2.3 Derivation of κ_{AMS}

κ_{AMS} is derived using the PTOF size-resolved mass observations. The mass distributions are first smoothed with a boxcar filter with a window of 10 size bins to reduce

noise. Although these are size-resolved measurements, mixing-state information is not obtained. The AMS is also limited to measurement of non-refractory material; refractory compounds (such as black carbon in soot and mineral dust) that do not vaporize in the AMS are not detected.
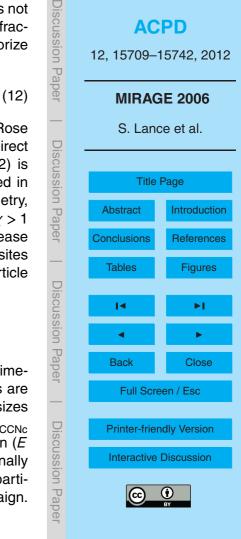
$$\kappa_{AMS} = f_{org}\kappa_{org} + (f_{NH_4} + f_{SO_4} + f_{NO_3})\kappa_{inorg} \tag{12}$$

We assume that $\kappa_{org} = 0.1$ and $\kappa_{inorg} = 0.65$, following other megacities studies (Rose et al., 2011; Gunthe et al., 2011). Since the AMS measurements do not provide direct evidence of the aerosol mixing-state, another underlying assumption in Eq. (12) is that no refractory material, and that all non-refractory material, is internally-mixed in the CCN-active aerosol population. Also note that soot often has a fractal geometry, especially in the size range of interest, which will result in a dynamic shape factor $\chi > 1$ and $d_{va} < \rho_p d_p$ (DeCarlo et al., 2004; Slowik et al., 2004). Thus, a measured increase in organic mass fraction at smaller particle sizes, as observed at the T0 and T1 sites during the MCMA-2003 campaign (Salcedo et al., 2006), may be partly due to particle shape effects that are unaccounted for.

3 Results

The aerosol water uptake properties during MIRAGE 2006 are summarized by a time-series of HTDMA and CCNc observations in Fig. 1. Dry particle size distributions are also shown (Fig. 1f), with horizontal lines indicating the lower and upper particle sizes in our analysis. κ_{CCNc} for 100 nm particles is 0.2±0.1 during MIRAGE 2006, and κ_{CCNc} is often higher for particles smaller than 100 nm (Fig. 1c). The CCN-active fraction (E from Eq. 1) is typically >70 % for particle sizes >40 nm (Fig. 1b), but occassionally drops to 40 % and lower. The hygroscopic growth factors for 100 nm and 40 nm particles (Fig. 1d, and e, respectively), vary between 1.0 and 1.8 throughout the campaign.
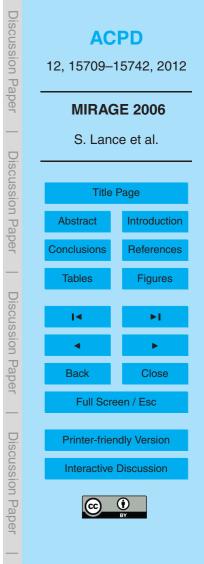
3.1 Diurnal changes in aerosol hygroscopicity

The dominant trend in Fig. 1 is a daily maximum in hygroscopic growth factor and κ_{CCNc} during the daytime. Figure 2 shows the mixing-state parameters from the CCN activation spectra. Both parameters in Fig. 2 are independently derived in our analysis, but both show strong diurnal trends. During the daytime, the fraction of CCN-active particles increases, coinciding with an increase in CCN hygroscopicity. There is a strong size dependence for both of these trends, with 40 nm particles exhibiting higher κ_{CCNc} but lower CCN-active fraction throughout most of the day. However, during the later half of the daylight hours, the CCN-active fraction for all particle sizes approaches 100 %.

κ_{CCNc} for all particle sizes reaches a maximum within 1–2 h of local noon, suggesting that photochemical processes are dominant, which is consistent with the peak in oxygenated organic aerosol mass (Aiken et al., 2009) and water soluble organic carbon mass (Hennigan et al., 2008) observed during the daytime at the T0 and T1 sites, respectively. A frequent occurrence during MIRAGE 2006 was new particle formation (NPF) events (Smith et al., 2008), as seen in the particle size distributions (Fig. 1f). The days with the strongest NPF events at the T1 site were the 16, 18, 21, 23, and 24 March (Fig. 3). Weaker and shorter-lived NPF events occured on almost all other days throughout the campaign. In the following analysis, we include only the five days with the strongest NPF events to represent NPF days, and contrast these days with all other days during the campaign.

The diurnal pattern of aerosol mixing-state is also influenced by breakup of the boundary layer and changes in emissions throughout the day. During 06:00–08:00 local time, there is a dramatic decrease in the CCN-active fraction for all particle sizes (Fig. 2), consistent with the greater vehicular emissions during the early morning rush hour and a low boundary layer height (Cross et al., 2009; Velasco et al., 2009; Aiken et al., 2009; Bon et al., 2011; Kalafut-Pettibone et al., 2011). A greater effect of primary motor vehicle emissions on particle sizes <60 nm is consistent with emission factors that peak in the 25–32 nm size range (Kalafut-Pettibone et al., 2011).

The ambient CCN concentration ($n_{CCN}(d_p, s) = dN_{CCN}/dlog d_p$) typically peaks during the daytime, consistent with previous studies in Mexico City (Baumgardner et al., 2004). Smaller particles exhibit greater diurnal changes in n_{CCN}. Figure 4 shows the average n_{CCN} on NPF days compared to all other days, as a function of the lo-
5   cal time of day and as a function of particle size. During the daytime on NPF days, $n_{CCN}(40\,nm, 0.5\,\%)$ is often more than a factor of two greater than $n_{CCN}(100\,nm, 0.5\,\%)$. On days without strong NPF events n_{CCN} remains relatively constant throughout the day. The biggest difference in n_{CCN} between NPF days and all other days occurs at successively later times during the day as particle size increases from 40 to 100 nm.
10   The increase in κ_{CCNc} during the daytime is also observed with κ_{HTDMA} (Fig. 5a). However, the nearly constant offset for κ_{CCNc} as a function of particle size is not observed with the HTDMA measurements. κ_{CCNc} and κ_{HTDMA} agree well for 100 nm particles (Fig. 5a), but $\kappa_{CCNc} \gg \kappa_{HTDMA}$ for 40 nm particles. Differences between subsaturated and supersaturated hygroscopicity may occur, especially at high f_{org}, if aerosol
15   constituents are slightly soluble or if they depress surface tension, which depends on the aerosol dilution (Padró et al., 2010).

3.2 Aerosol chemical composition

The size-resolved AMS measurements show that the organic mass fraction (f_{org}) is typically >50 % for all particle sizes analyzed, and regularly approaches 100 % during
20   the morning for 40 nm particles (Fig. 5b). The diurnal profile shows a decrease in f_{org} during the daytime for all particle sizes. f_{org} for 40 nm particles remains high for ∼2 additional hours in the morning, compared to the other particle sizes.
An inverse relationship is observed between κ_{CCNc} and f_{org} (Fig. 6), which typically falls within the range from several other studies (Dusek et al., 2010; Rose et al.,
25   2011; Gunthe et al., 2011; Cerully et al., 2011). For 100 nm particles $\kappa_{inorg} = 0.46$ and $\kappa_{org} = 0.04$, while for 40 nm particles $\kappa_{inorg} = 0.94$ and $\kappa_{org} = 0.21$. κ_{inorg} for the MIRAGE 2006 dataset increases for smaller particle sizes, but the variability and uncertainty increase as well. The 100 nm observations are more robust than the 40 nm observations,

because two independent datasets yield comparable values for κ^* (Fig. 5a), and also because the mass of 100 nm particles is typically much greater than for 40 nm particles, resulting in much lower uncertainty for f_{org}.
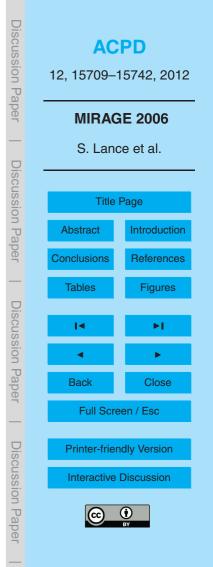
3.3 Averaging by Time Period

To further highlight the dominant factors influencing the evolution of the aerosol mixing-state throughout the day, we average the distributions of supersaturated and subsaturated hygroscopicity during MIRAGE 2006 over different time periods: (1) daytime (08:00–16:00 local time) on NPF days, (2) daytime on all other days, (3) all times of day over the whole campaign, and (4) during the early morning rush hour (06:00–08:00 local time). Since these are size resolved measurements, changes in the CCN activation spectra and GF distributions during different time periods are due to changes in the aerosol chemical composition and mixing-state.

NPF events and primary vehicular emissions often exhibit competing effects on the CCN-active fraction, especially for smaller particles. The greater effect of both NPF events and the morning rush hour on smaller particles is not surprising since NPF leads to a strong Aitken mode and since primary motor vehicle emissions during MIRAGE peak in number concentration in the 25–32 nm size range (Kalafut-Pettibone et al., 2011). For all particle sizes, the fraction of particles in the nonhygroscopic mode (GF centered at 1.0±0.03) is highest during the early morning rush hour, and lowest during the daytime on NPF days (Fig. 7e–h). The CCN-active fractions are also at their lowest and highest, respectively, during these time periods (Fig. 7a–d). The greatest change in the hygroscopicity of the CCN-active aerosol population occurs between the morning rush hour and the daytime on NPF days (Fig. 7). The hygroscopic mode during the morning rush hour becomes more hygroscopic during the daytime on NPF days, increasing from a mean modal GF of 1.34–1.41 to 1.48–1.51, while s^* changes by as much as 20 % on average between these two time periods.

The increase in hygroscopicity for the CCN-active population during the daytime may be due to several different mechanisms: (1) growth of new particles during NPF events

(by coagulation with other newly formed particles or by condensational growth of secondary species), (2) growth of primary particles by coagulation with particles formed during NPF events, (3) growth of primary particles by condensation of secondary species, and (4) photo-oxidation of constituents already present within the aerosol. It is not simple to evaluate which of these mechanism(s) are playing a dominant role, since several or all of them may be acting at the same time. However, the water uptake distributions provide several clues. For 100 nm particles, the CCN activation spectra (Fig. 7a) and the GF distributions (Fig. 7e, i) are nearly the same during the daytime whether or not strong NPF events occur. This suggests that the third and/or fourth mechanism(s) have a dominant impact on the observed diurnal trend for 100 nm particles. For 40–80 nm particles, although the CCN-active fraction remains the same during the daytime whether or not NPF events occur, the chemical heterogeneity of the CCN decreases during NPF events, as evidenced by both greater slopes for the CCN activation spectra and narrower GF distributions. This implies a greater impact from NPF events for this size range, and therefore a greater role for the first and/or second mechanisms. However, the third and fourth mechanisms may play an important role for 40–80 nm particles on days when strong NPF events do not occur, since primary particles in the nonhygroscopic mode that are present in the morning apparently attain soluble material during the daytime (as evidenced by a distinct GF mode at 1.2 with simultaneous loss of the nonhygroscopic mode, Fig. 7j–l). On NPF days, the third and fourth mechanisms appear to be less important for 40–80 nm particles due to less significant contribution of aged primary particles compared to the concentration of newly formed particles.

The increase in both κ_{CCNc} and κ_{HTDMA} during NPF events is contrary to the observations of Dusek et al. (2010), where NPF was shown to increase organic mass fraction and decrease hygroscopicity. This is in spite of the fact that f_{org} is typically >0.5 for all particle sizes during the daytime in Mexico City and the fact that organics were shown to contribute substantially to the growth of particles 10–35 nm during NPF events (Smith et al., 2008).
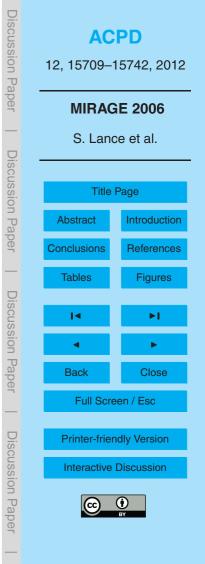
Figure 8 shows the average aerosol composition, hygroscopicity and mixing-state observations as a function of particle size for the same specified time periods as in Fig. 7. The dominant trends are an increase in CCN-active fraction and a decrease in f_{org} with particle size (Fig. 8a). Differences in mixing-state could explain why κ_{CCNc} does not follow the same trend as κ_{AMS}; for all time periods, κ_{CCNc} decreases with particle size, whereas κ_{AMS} remains constant or increases with size (Fig. 8b). An external mixture of measured organic compounds (assumed to be internally-mixed in calculation of κ_{AMS}) would result in $\kappa_{AMS} < \kappa_{CCNc}$. Evidence for this occurring is the fact that when the CCN-active fraction for 40 nm particles approaches 1.0 (i.e. during the daytime and especially during NPF events), κ_{AMS} approaches κ_{CCNc}. Increasing κ_{inorg} by a small and realistic amount (from 0.65 to 0.7) in calculation of κ_{AMS} would reduce the discrepancy with κ_{CCNc} further. However, when the CCN-active fraction for 40 nm particles is only 0.5 (i.e. during the early morning rush hour) $\kappa_{AMS} \ll \kappa_{CCNc}$, which is also consistent with this hypothesis, suggesting that much of the measured organic mass is externally-mixed to the CCN-active aerosol population during this time period. Conversely, an internal mixture of refractory components (not measured by the AMS) would explain why $\kappa_{AMS} > \kappa_{CCNc}$, as seen for 100 nm particles during all time periods. Single particle measurements at the T1 site show that primary particles >350 nm d_{va} containing hydrocarbon-like organic aerosol (HOA) compounds linked to combustion sources "became internally mixed particles (i.e. were coated with photochemical products) in ~15–30 min during the mid to late morning (09:00–12:00 [local time])" (Cross et al., 2009). Although the single particle measurements represent particles that are at least two times larger than the 100 nm particles in our analysis, it does provide further support to the hypothesis that the externally-mixed primary particles emitted during the morning rush hour rapidly grow into larger particles, either through condensation of secondary inorganic and organic species, or by coagulation with other particles, leading to larger particles that are internally-mixed (and likely contain refractory material).

3.4 Effect of Mixing-State on CCN concentrations

To evaluate the impact of mixing-state and composition on the observed CCN concentrations, we calculate CCN activation spectra with different assumptions for E, σ_κ and κ^*. The simulated activat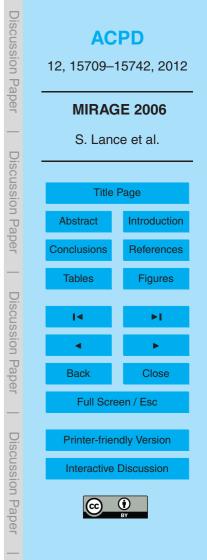ion spectra are then multiplied by the measured classified particle concentrations to determine the calculated CCN concentrations, which are then compared to measured CCN concentrations for the full range of supersaturations. First, we constrain the simulated CCN activation spectra with κ_{CCNc}, E and σ_κ, as determined from the CCN measurements, to evaluate the uncertainty in the method, yielding linear correlation coefficients of $R^2 = 0.949$–0.990, and slopes of 0.945–0.996 for calculated versus measured CCN concentrations (Fig. 9a). Uncertainty in calculated CCN concentrations constrained by these CCNc-derived parameters arises mainly from variability in the activation spectra for timescales <30 min or >16 s, which manifests as random scatter of the observed $R_a(S)$ about the sigmoidal fits.

Next we assume that $\kappa^* = \kappa_{AMS}$. Despite clear differences in κ^* derived independently from CCNc and AMS data (Fig. 8b), we find that measured CCN concentrations can be reasonably described using κ_{AMS}, yielding linear correlation coefficients of $R^2 = 0.634$–0.953, and slopes of 0.825–1.04 (Fig. 9b). Since κ_{AMS} tends to be $>\kappa_{CCNc}$ for 100 nm particles, the calculated CCN concentrations tend to be greater than observed CCN concentrations, yielding the highest slope in this range. Since κ_{AMS} tends to be $<\kappa_{CCNc}$ for 40 nm particles, the calculated CCN concentrations tend to be lower than observed CCN concentrations, yielding the lowest slope in this range.

Finally, to evaluate the effect of mixing-state on measured CCN concentrations, we assume that $E = 1.0$ and $\sigma_\kappa = 0$, yielding linear correlation coefficients of $R^2 = 0.822$–0.931, and slopes of 1.06–1.09 (Fig. 9c). By analyzing the data as a function of the local time of day, we find that mixing-state information is important for describing CCN concentrations during the morning rush hour, when E is often $\leq\sim0.8$. Under these conditions, the calculated CCN concentrations often overestimate the measured CCN concentrations by 50–100 %. At the highest CCN concentrations (≥500 cm^{-3}, calculated

CCN concentrations agree well with measured concentrations because the highest CCN concentrations occur during the daytime as a result of NPF events when E approaches 1.0 and when the chemical heterogeneity of the CCN-active aerosol population is at a minimum.
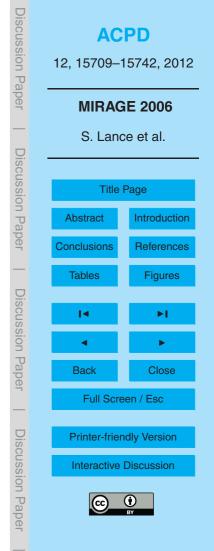
4 Conclusions

We obtained CCN activation spectra for a two week ground-based study at the T1 site outside of Mexico City during MIRAGE 2006, from which the size-resolved chemical composition and mixing-state of particles 40–100 nm is inferred. Aerosol hygroscopicity was simultaneously measured with a HTDMA covering the same particle size range. The major trend observed is a diurnal pattern with greater concentration and fraction of CCN during the daytime and also greater characteristic hygroscopicity parameter, κ^*, during the daytime. New particle formation events and the daily early morning rush hour are found to have dominant influences on the aerosol composition and mixing-state in the studied size range. κ^* is compared to size resolved organic mass fraction, and a linear fit is obtained, with lower slope than observed in several other studies. Comparisons with HTDMA data rule out the likelihood of measurement artifact causing this lower slope.

κ^* derived from bulk aerosol composition measurements implies constant or increasing hygroscopicity with size, in contrast with the water uptake measurements. We present evidence that externally-mixed nonrefractory material (which is measured by the AMS but does not affect the CCN-active aerosol population) can explain why $\kappa_{CCNc} > \kappa_{AMS}$ for smaller particles, while internally-mixed refractory material (which is not measured by the AMS but does affect the CCN-active aerosol population) can explain why larger particles exhibit $\kappa_{AMS} > \kappa_{CCNc}$.

In conclusion, we find that CCN concentrations can often be described well using either κ_{AMS} or κ_{CCNc}, without considering the aerosol chemical heterogeneity, but only when the CCN-active fraction is $> \sim 0.8$. During the early morning rush hour, the CCN-

active fraction was often <0.8, and CCN concentrations were often overpredicted by 50–100 % when the aerosol mixing-state was not considered.

Disclaimer

References

Aiken, A. C., Salcedo, D., Cubison, M. J., Huffman, J. A., DeCarlo, P. F., Ulbrich, I. M., Docherty, K. S., Sueper, D., Kimmel, J. R., Worsnop, D. R., Trimborn, A., Northway, M., Stone, E. A., Schauer, J. J., Volkamer, R. M., Fortner, E., de Foy, B., Wang, J., Laskin, A., Shutthanandan, V., Zheng, J., Zhang, R., Gaffney, J., Marley, N. A., Paredes-Miranda, G., Arnott, W. P., Molina, L. T., Sosa, G., and Jimenez, J. L.: Mexico City aerosol analysis during MILAGRO using high resolution aerosol mass spectrometry at the urban supersite (T0) – Part 1: Fine particle composition and organic source apportionment, Atmos. Chem. Phys., 9, 6633–6653, doi:10.5194/acp-9-6633-2009, 2009 15722
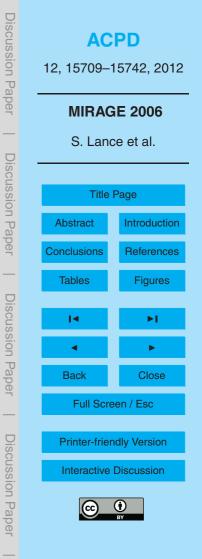
Andreae, M. O. and Rosenfeld, D.: Aerosol-cloud-precipitation interactions – Part 1: The nature and sources of cloud-active aerosols, Earth-Sci. Rev., 89, 13–41, 2008. 15713

Ashkar, F. and Mahdi, S.: Fitting the log-logistic distribution by generalized moments, J. Hydrol., 328, 694–703, 2006. 15716, 15717, 15719

Baumgardner, D., Raga, G. B., and Muhlia, A.: Evidence for the formation of CCN by photochemical processes in Mexico City, Atmos. Environ., 38, 357–367, 2004. 15723

Bon, D. M., Ulbrich, I. M., de Gouw, J. A., Warneke, C., Kuster, W. C., Alexander, M. L., Baker, A., Beyersdorf, A. J., Blake, D., Fall, R., Jimenes, J. L., Herndon, S. C., Huey, L. G., Knighton, W. B., Ortega, J., Springston, S., and Vargas, O.: Measurements of volatile organic compounds at a suburban ground site (T1) in Mexico City during the MILAGRO 2006 campaign: measurement comparison, emission ratios, and source attribution, Atmos. Chem. Phys., 11, 2399–2421, doi:10.5194/acp-11-2399-2011, 2011. 15722

Cerully, K. M., Raatikainen, T., Lance, S., Tkacik, D., Tiitta, P., Petäjä, T., Ehn, M., Kulmala, M., Worsnop, D. R., Laaksonen, A., Smith, J. N., and Nenes, A.: Aerosol hygroscopicity and CCN activation kinetics in a Boreal forest environment during the 2007 EUCAARI Campaign, Atmos. Chem. Phys., 11, 12369–12386, doi:10.5194/acp-11-12369-2011, 2011. 15713, 15717, 15723

Chen, D.-R., Pui, D. Y. H., Hummes, D., Fissan, H., Quant, F. R., and Sem, G. J.: Design and evaluation of a nanometer aerosol differential mobility analyzer (Nano-DMA), J. Aerosol Sci., 29, 497–509, 1998. 15713

Cross, E. S., Onasch, T. B., Canagaratna, M., Jayne, J. T., Kimmel, J., Yu, X.-Y., Alexander, M. L., Worsnop, D. R., and Davidovits, P.: Single particle characterization using a light scattering module coupled to a time-of-flight aerosol mass spectrometer, Atmos. Chem. Phys., 9, 7769–7793, doi:10.5194/acp-9-7769-2009, 2009. 15715, 15722, 15726

DeCarlo, P. F., Slowik, J. G., Worsnop, D. R., Davidovits, P., and Jimenez, J. L.: Particle morphology and density characterization by combined mobility and aerodynamic diameter measurements – Part 1: Theory, Aeros. Sci. Technol., 38, 1185–1205, doi:10.1080/027868290903907, 2004. 15716, 15721

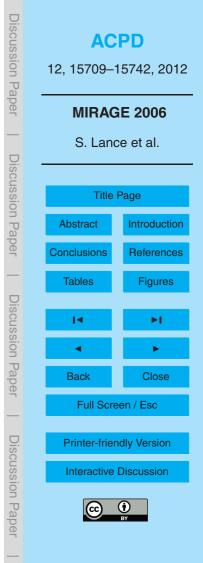Dusek, U., Frank, G. P., Curtius, J., Drewnick, F., Schneider, J., Kürten, A., Rose, D., Andreae, M. O., Borrmann, S., and Pöschl, U.: Enhanced organic mass fraction and decreased hygroscopicity of cloud condensation nuclei (CCN) during new particle formation events, Geophys. Res. Lett., 37, L03804, doi:10.1029/2009GL040930, 2010. 15723, 15725

Title Page

Abstract | Introduction

Conclusions | References

Tables | Figures

◄◄ | ►►

◄ | ►

Back | Close

Full Screen / Esc

Printer-friendly Version

Interactive Discussion

Fast, J. D., de Foy, B., Acevedo Rosas, F., Caetano, E., Carmichael, G., Emmons, L., McKenna, D., Mena, M., Skamarock, W., Tie, X., Coulter, R. L., Barnard, J. C., Wiedinmyer, C., and Madronich, S.: A meteorological overview of the MILAGRO field campaigns, Atmos. Chem. Phys., 7, 2233–2257, doi:10.5194/acp-7-2233-2007, 2007. 15712

Gunthe, S. S., Rose, D., Su, H., Garland, R. M., Achtert, P., Nowak, A., Wiedensohler, A., Kuwata, M., Takegawa, N., Kondo, Y., Hu, M., Shao, M., Zhu, T., Andreae, M. O., and Pöschl, U.: Cloud condensation nuclei (CCN) from fresh and aged air pollution in the megacity region of Beijing, Atmos. Chem. Phys., 11, 11023–11039, doi:10.5194/acp-11-11023-2011, 2011. 15721, 15723

Hennigan, C. J., Sullivan, A. P., Fountoukis, C. I., Nenes, A., Hecobian, A., Vargas, O., Peltier, R. E., Case Hanks, A. T., Huey, L. G., Lefer, B. L., Russell, A. G., and Weber, R. J.: On the volatility and production mechanisms of newly formed nitrate and water soluble organic aerosol in Mexico City, Atmos. Chem. Phys., 8, 3761–3768, doi:10.5194/acp-8-3761-2008, 2008. 15722

Jayne, J. T., Leard, D. C., Zhang, X., Davidovits, P., Smith, K. A., Kolb, C. E., and Worsnop, D. R.: Development of an aerosol mass spectrometer for size and composition analysis of submicron particles, Aeros. Sci. Technol., 33, 49–70, 2000. 15715

Kalafut-Pettibone, A. J., Wang, J., Eichinger, W. E., Clarke, A., Vay, S. A., Blake, D. R., and Stanier, C. O.: Size-resolved aerosol factors and new particle formation/growth activity occurring in Mexico City during the MILAGRO 2006 Campaign, Atmos. Chem. Phys., 11, 8861–8881, doi:10.5194/acp-11-8861-2011, 2011. 15722, 15724

Lance, S.: Quantifying compositional impacts of ambient aerosol on cloud droplet formation, Published Doctoral Thesis, available at: http://etd.gatech.edu/theses/available/etd-11132007-175217/unrestricted/lance_sara_m_200712_phd[1].pdf, 2007. 15717

Lance, S., Medina, J., Smith, J. N., and Nenes, A.: Mapping the Operation of the DMT Continuous Flow CCN Counter, Aerosol Sci. Technol., 40, 242–254, doi:10.1080/02786820500543290, 2006. 15713

Lathem, T. L. and Nenes, A.: Water vapor depletion in the DMT continuous flow CCN chamber: Effects on supersaturation and droplet growth, Aerosol Sci. Technol., 45, doi:10.1080/02786826.2010.551146, 2011. 15714
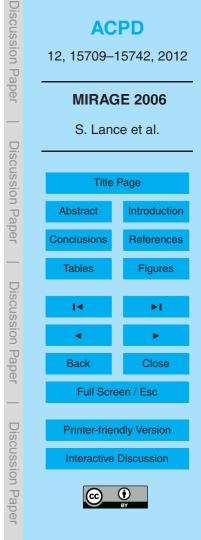
McMurry, P. H., Ghimire, A., Ahn, K.-H., Sakurai, H., Stolzenburg, M., and Smith, J. N.: Sampling nanoparticles for chemical analysis by low resolution electrical mobility classification, Environ. Sci. Technol., 43, 4653–4658, doi:10.1021/es8029335, 2009. 15714

MIRAGE 2006

S. Lance et al.

Title Page

Abstract | Introduction

Conclusions | References

Tables | Figures

◄ | ►

◄ | ►

Back | Close

Full Screen / Esc

Printer-friendly Version

Interactive Discussion

Molina, L. T., Madronich, S., Gaffney, J. S., Apel, E., de Foy, B., Fast, J., Ferrare, R., Herndon, S., Jimenez, J. L., Lamb, B., Osornio-Vargas, A. R., Russell, P., Schauer, J. J., Stevens, P. S., Volkamer, R., and Zavala, M.: An overview of the MILAGRO 2006 Campaign: Mexico City emissions and their transport and transformation, Atmos. Chem. Phys., 10, 8697–8760, doi:10.5194/acp-10-8697-2010, 2010. 15712

Padró, L. T., Tkacik, D., Lathem, T., Hennigan, C. J., Sullivan, A. P., Weber, R. J., Huey, L. G., and Nenes, A.: Investigation of cloud condensation nuclei properties and droplet growth kinetics of the water soluble aerosol fraction in Mexico City, J. Geophys. Res., 150, 2010. 15718, 15723

Petters, M. D., and Kreidenweis, S. M., A single parameter representation of hygroscopic growth and cloud condensation nucleus activity, Atmos. Chem. Phys., 7, 1961–1971, doi:10.5194/acp-7-1961-2007, 2007. 15715, 15717, 15719

Rader, D. J. and McMurry, P. H.: Application of the tandem differential mobility analyzer to studies of droplet growth or evaporation, J. Aerosol Sci., 17, 771–787, 1986. 15715, 15719, 15720

Roberts, G. C., and Nenes, A.: A continuous-flow streamwise thermal-gradient CCN chamber for atmospheric measurements, Aerosol Sci. Technol., 39, 206–221, 2005. 15713

Rose, D., Frank, G. P., Dusek, U., Gunthe, S. S., Andreae, M. O., and Pöschl, U.: Calibration and measurement uncertainties of a continuous-flow cloud condensation nuclei counter (DMT-CCNC): CCN activation of ammonium sulfate and sodium chloride aerosol particles in theory and experiment, Atmos. Chem. Phys., 8, 1153–1179, doi:10.5194/acp-8-1153-2008, 2008. 15713

Rose, D., Nowak, A., Achtert, P., Wiedensohler, A., Hu, M., Shao, M., Zhang, Y., Andreae, M. O., and Pöschl, U.: Cloud condensation nuclei in polluted air and biomass burning smoke near the mega-city Guangzhou, China – Part 1: Size-resolved measurements and implications for the modeling of aerosol particle hygroscopicity and CCN activity, Atmos. Chem. Phys., 10, 3365–3383, doi:10.5194/acp-10-3365-2010, 2010. 15714

Rose, D., Gunthe, S. S., Su, H., Garland, R. M., Yang, H., Berghof, M., Cheng, Y. F., Wehner, B., Achtert, P., Nowak, A., Wiedensohler, A., Takegawa, N., Kondo, Y., Hu, M., Zhang, Y., Andreae, M. O., and Pöschl, U.: Cloud condensation nuclei in polluted air and biomass burning smoke near the mega-city Guangzhou, China - Part 2: Size-resolved aerosol chemical composition, diurnal cycles, and externally mixed weakly CCN-active soot particles, Atmos. Chem. Phys., 11, 2817–2836, doi:10.5194/acp-11-2817-2011, 2011. 15721, 15723

MIRAGE 2006

S. Lance et al.

Title Page

Abstract | Introduction

Conclusions | References

Tables | Figures

◀ | ▶

◀ | ▶

Back | Close

Full Screen / Esc

Printer-friendly Version

Interactive Discussion

Salcedo, D., Onasch, T. B., Dzepina, K., Canagaratna, M. R., Zhang, Q., Huffman, J. A., De-Carlo, P. F., Jayne, J. T., Mortimer, P., Worsnop, D. R., Kolb, C. E., Johnson, K. S., Zuberi, B., Marr, L. C., Volkamer, R., Molina, L. T., Molina, M. J., Cardenas, B., Bernabé, R. M., Márquez, C., Gaffney, J. S., Marley, N. A., Laskin, A., Shutthanandan, V., Xie, Y., Brune, W., Lesher, R., Shirley, T., and Jimenez, J. L.: Characterization of ambient aerosols in Mexico City during the MCMA-2003 campaign with Aerosol Mass Spectrometry: results from the CENICA Supersite, Atmos. Chem. Phys., 6, 925–946, doi:10.5194/acp-6-925-2006, 2006. 15716, 15721

Seinfeld, J., and Pandis, S.: Atmospheric Chemistry and Physics: from Air Pollution to Climate Change, John Wiley, New York, USA, 1326 pp., 1998. 15714

Smith, J. N., Dunn, M. J., VanReken, T. M., Iida, K., Stolzenburg, M. R., McMurry, P. H., and Huey, L. G.: Chemical composition of atmospheric nanoparticles formed from nucleation in Tecamac, Mexico: Evidence for an important role for organic species in nanoparticle growth, Geophys. Res. Lett., 35, L04808, doi:10.1029/2007GL032523, 2008. 15722, 15725

Slowik, J. G., Stainken, K., Davidovits, P., Williams, L. R., Jayne, J. T., Kolb, C. E., Worsnop, R., Rudich, Y., DeCarlo, P. F., and Jimenez, J. L.: Particle morphology and density characterization by combined mobility and aerodynamic diameter measurements – Part 2: Application to combustion-generated soot aerosols as a function of fuel equivalence ratio, Aeros. Sci. Technol., 38, 1206–1222, 2004. 15721

Stolzenburg, M. R. and McMurry, P. H.: TDMAfit user's manual, Particle Technology Laboratory, Department of Mechanical Engineering, Univeristy of Minnesota, Minneapolis, MN, Publication No. 653, 1988. 15720

Su, H., Rose, D., Cheng, Y. F., Gunthe, S. S., Massling, A., Stock, M., Wiedensohler, A., Andreae, M. O., and Pöshcl, U.: Hygroscopicity distribution concept for measurement data analysis and modeling of aerosol particle mixing state with regard to hygroscopic growth and CCN activation, Atmos. Chem. Phys., 10, 7489–7503, doi:10.5194/acp-10-7489-2010, 2010. 15720

Velasco, E., Pressley, S., Grivicke, R., Allwine, E., Coons, T., Foster, W., Jobson, B. T., Westberg, H., Ramos, R., Hernández, F., Molina, L. T., and Lamb, B.: Eddy covariance flux measurements of pollutant gases in urban Mexico City, Atmos. Chem. Phys., 9, 7325–7342, doi:10.5194/acp-9-7325-2009, 2009. 15722

Title Page

Abstract | Introduction

Conclusions | References

Tables | Figures

|◀ | ▶|

◀ | ▶

Back | Close

Full Screen / Esc
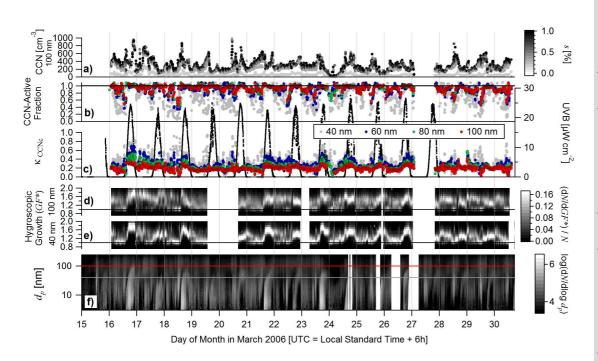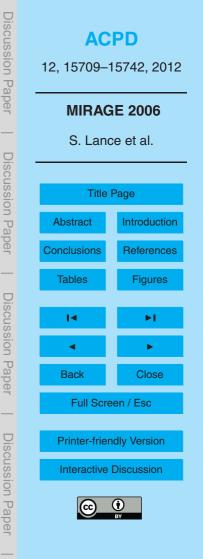
Printer-friendly Version

Interactive Discussion

Fig. 1. Overview timeseries of measured aerosol microphysical properties during the MIRAGE 2006 campaign: **(a)** number concentration of 100 nm particles acting as CCN, **(b)** fraction of particles acting as CCN at ~1 % supersaturation, **(c)** hygroscopicity parameter for the CCN-active fraction, hygroscopic diameter growth factor distribution for **(d)** 100 nm, and **(e)** 40 nm particles, and **(f)** aerosol size distribution for 3–250 nm particles, with 40 nm and 100 nm highlighted in grey and red, respectively. In **(b)** and **(c)**, parameters are reported for 40, 60, 80 and 100 nm paricles. The growth factor distributions in **(d)** and **(e)** are normalized to particle number concentrations.
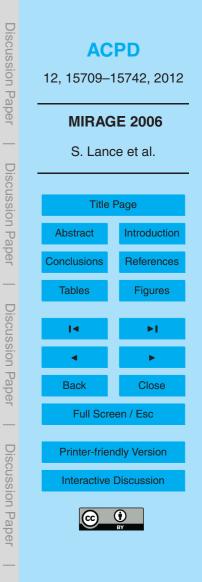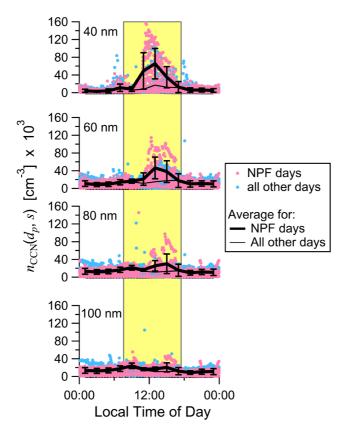
Fig. 2. Average diurnal profile of measured mixing-state properties and composition of 40, 60, 80 and 100 nm aerosol during the MIRAGE 2006 campaign: **(a)** fraction of particles acting as CCN at ~1 % supersaturation, **(b)** hygroscopicity parameter for the CCN-active fraction. Plotted on the right axis is a Gaussian fit to the average ultraviolet solar intensity (UVB) as a function of the local time of day (UTC − 6 h) during MIRAGE 2006, with the daylight hours between 07:36 and 17:27 (±5 h from solar maximum) highlighted.
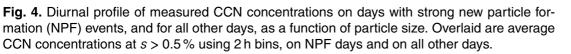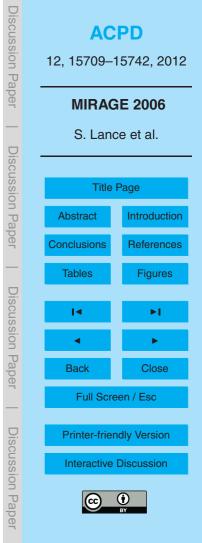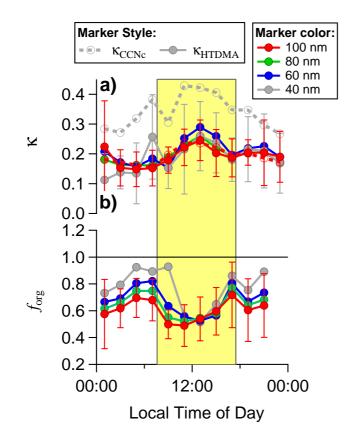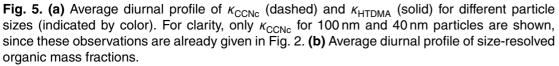
Fig. 3. Particle size distributions on "NPF days", days during which strong new particle formation events occurred.

Fig. 4. Diurnal profile of measured CCN concentrations on days with strong new particle formation (NPF) events, and for all other days, as a function of particle size. Overlaid are average CCN concentrations at $s > 0.5\%$ using 2 h bins, on NPF days and on all other days.

Fig. 5. (a) Average diurnal profile of κ_{CCNc} (dashed) and κ_{HTDMA} (solid) for different particle sizes (indicated by color). For clarity, only κ_{CCNc} for 100 nm and 40 nm particles are shown, since these observations are already given in Fig. 2. **(b)** Average diurnal profile of size-resolved organic mass fractions.
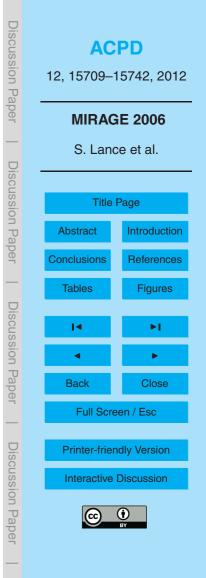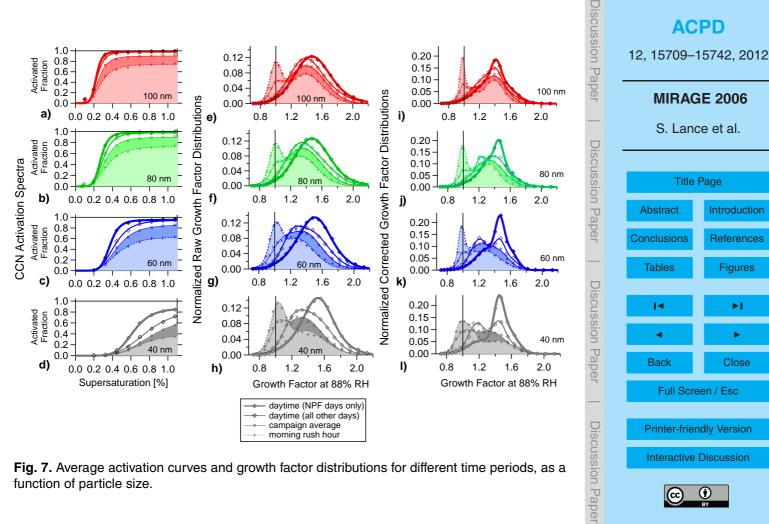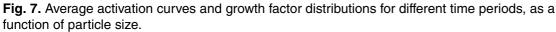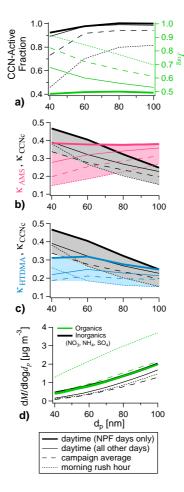
Fig. 6. κ_{CCNc} versus organic mass fraction, as a function of particle diameter. Linear fits as a function of particle size are shown with solid colored lines. Also shown are linear fits found in other polluted and remote environments.
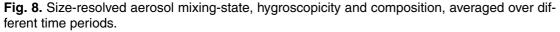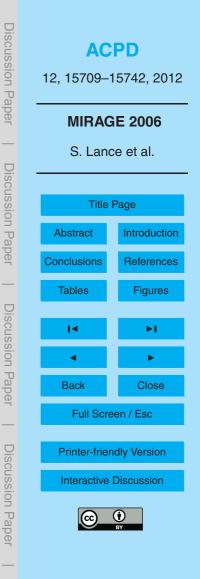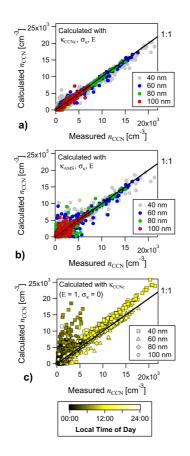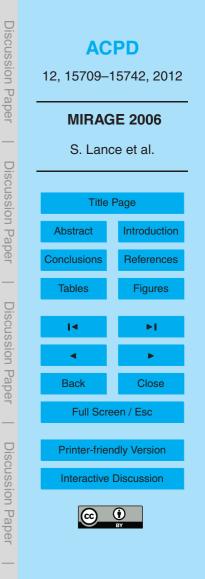
Fig. 7. Average activation curves and growth factor distributions for different time periods, as a function of particle size.

Fig. 8. Size-resolved aerosol mixing-state, hygroscopicity and composition, averaged over different time periods.

[ACPD](#)

12, 15709–15742, 2012

MIRAGE 2006

S. Lance et al.

Title Page

Abstract | Introduction

Conclusions | References

Tables | Figures

◄ | ►

◄ | ►

Back | Close

Full Screen / Esc

Printer-friendly Version

Interactive Discussion

Fig. 9. CCN concentrations calculated from three different methods: **(a)** using d_p, σ_{d_p}, κ_{CCNc}, E and σ_κ; **(b)** the same as in **(a)** but using κ_{AMS} instead of κ_{CCNc}; and **(c)** the same as in **(a)** but not accounting for the aerosol chemical heterogeneity ($E = 1$ and $\sigma_\kappa = 0$). Calculated CCN concentrations are compared to measured CCN concentrations for a given classified particle size. Markers are colored by local time of day in **(c)**.